



Numerical investigation of droplet motion and coalescence by an improved lattice Boltzmann model for phase transitions and multiphase flows

Shuai Gong, Ping Cheng*

Ministry of Education Key Laboratory for Power Machinery and Engineering, Shanghai Jiao Tong University, Shanghai 200240, PR China

ARTICLE INFO

Article history:

Received 14 April 2011

Received in revised form 31 August 2011

Accepted 28 September 2011

Available online 5 October 2011

Keywords:

Droplet movement

Multiphase flows

Lattice Boltzmann method

Wettability

ABSTRACT

An improved model for simulation of phase transitions and single-component multiphase flows by lattice Boltzmann method is proposed and developed in this paper. It is shown that both the scheme for the interparticle interaction force term and the method of incorporating the force term are important for obtaining accurate and stable numerical results for simulations of single-component multiphase flows. A new scheme for the force term is proposed and simulation results of several non-ideal equation of state suggest that the proposed scheme can greatly improve the coexistence curves. Among several methods of incorporating the force term, the exact difference method is shown to have better accuracy and stability. Furthermore, it avoids the unphysical phenomenon of relaxation time dependence. Compared with existing models, the proposed model, consisting of the new force term scheme together with the exact difference method to incorporate the force term, can give more accurate and stable numerical results in a wider temperature range with the spurious currents greatly reduced. Droplet motion and coalescence processes on surfaces with wettability gradients are numerically investigated based on the newly proposed model. The velocity field and mechanism of droplet motion are illustrated in details.

© 2011 Elsevier Ltd. All rights reserved.

1. Introduction

A great deal of studies on multiphase flows have been done during the past several decades, and they have attracted much attention recently because of their important applications in micro thermo-fluidics devices [1–3]. In particular, the lattice Boltzmann method (LBM) has shown great potentials in modeling complex fluid systems. Differing from conventional macroscopic schemes based on discretizations of macroscopic continuum equations, LBM is based on mesoscopic kinetic equations and can incorporate interparticle interactions directly. Due to its kinetic nature and no need to track the interface explicitly, LBM has been found to be an effective tool for numerical solutions of problems involving interfacial dynamics (such as multiphase/multicomponent flows) and complex boundaries (such as porous media).

Several LBM multiphase/multicomponent models have been proposed during the past two decades [4–6]. The pseudo-potential model by Shan and Chen [4] (S–C model) and the free energy model by Swift et al. [5] are two major models, both of which have sound physical bases. In the S–C model, interparticle interactions between neighboring lattices, represented by a pseudo-potential function, are introduced to account for the phase transition and the non-ideal equation of state. Phase separation occurs automatically and it is not

necessary to track the interface. So the computation cost is lower than interface capturing methods such as VOF [7] and level set [8]. Moreover, different wetting conditions can be conveniently implemented by adjusting the interaction strength between fluid particles and the solid wall. Another advantage of this model is that any equation of state can easily be incorporated, and this is crucial in many industrial applications involving real gases. One drawback of the pseudo-potential model is that the local momentum of each lattice is not conserved, although the total momentum conservation is indeed satisfied. The free energy model proposed by Swift et al. satisfies the local momentum conservation, and thermodynamic consistency is ensured by introducing a non-ideal pressure tensor [5]. However, this model suffers from a lack of Galilean invariance and it has only been used in connection with the van der Waals (vdW) equation of state.

After the single component multiphase S–C model was proposed by Shan and Chen [4] in 1993, several other groups [9–11] have proposed variants of this model. Yuan and Schaefer [9] investigated the incorporation of various equations of state into the pseudo-potential model. They focused their attention on the density ratios, spurious currents and temperature ranges of different equations of state. Their results suggested that performances of the pseudo-potential model, such as the maximum density ratio, spurious currents, and the temperature range, depend on the particular equation of state used. For example, for vdW equation of state, stable solutions can only be obtained for a density ratio less

* Corresponding author. Tel./fax: +86 21 3420 6337.

E-mail address: pingcheng@sjtu.edu.cn (P. Cheng).

than 7.2 due to the large spurious currents. On the other hand, using equations of state by Peng–Robinson (P–R) and Carnahan–Starling (C–S), stable solutions can be obtained for a density ratio as high as 1000. Zhang and Chen [10] proposed a new scheme of the force term and adopted a different method to incorporate the force term into their model. Recently, Zeng et al. [11] proposed a new model by combining the force term scheme in Zhang and Chen [10] model together with the force incorporation method in S–C model [4]. However, simulation results based on vdW equation of state suggested that the performance of this model was only slightly improved.

All of the above mentioned models have some drawbacks. Simulation results of the densities (especially for the vapor branch) deviate from analytical solutions based on the Maxwell construction drastically at low temperatures. Small temperature ranges in which these models can have stable numerical results are another drawback. Furthermore, densities of the two phases depending on the relaxation time given by some existing models are physically unrealistic. For the above reasons, further studies for improved multiphase LBM are needed.

In this paper, a new scheme for the interparticle interaction force term, based on the modification of the S–C force model [4], is proposed. This together with the exact difference method [12] for incorporating the new force term scheme is developed as the new multiphase LBM model. Compared with other existing models, the proposed model not only gives more accurate and stable simulation results in a much wider temperature range but also avoids the physically unrealistic phenomenon of relaxation time dependence.

2. Model description

In this section, we will first give a brief introduction to LBM, and review several existing schemes for interparticle interaction force terms [4,9–11] and methods for incorporating these interparticle interaction force terms [4,12–16] in LBM. Finally, an improved interparticle interaction force term scheme based on the modification of the S–C model is proposed.

2.1. The lattice Boltzmann method

In LBM, the fluid is described by the evolution of microscopic fluid particles or particle distribution functions. The evolution equation of the particle distribution function with the BGK collision operator [17] is governed by

$$f_i(\mathbf{x} + \mathbf{e}_i \delta_t, t + \delta_t) - f_i(\mathbf{x}, t) = -\frac{1}{\tau} (f_i(\mathbf{x}, t) - f_i^{(eq)}(\mathbf{x}, t)) + \Delta f_i(\mathbf{x}, t) \quad (1)$$

where $f_i(\mathbf{x}, t)$ is the particle distribution function with velocity \mathbf{e}_i at position \mathbf{x} and time t , τ the relaxation time, $\Delta f_i(\mathbf{x}, t)$ the body force term such as gravity or electric forces [18] and $f_i^{(eq)}(\mathbf{x}, t)$ the corresponding equilibrium distribution function given by

$$f_i^{(eq)} = \omega_i \rho \left[1 + \frac{\mathbf{e}_i \cdot \mathbf{u}}{c_s^2} + \frac{(\mathbf{e}_i \cdot \mathbf{u})^2}{2c_s^4} - \frac{\mathbf{u}^2}{2c_s^2} \right] \quad (2)$$

where ω_i are the weighting coefficients and c_s is the lattice sound speed. For 2D and 3D simulations, we choose the D2Q9 and D3Q19 schemes, respectively. For D2Q9 lattice, the weighting coefficients ω_i are given by $\omega_i = 4/9$ for $i = 0$; $\omega_i = 1/9$ for $i = 1-4$ and $\omega_i = 1/36$ for $i = 5-8$. And the discrete velocity vectors are given as follows

$$\mathbf{e}_i = \begin{cases} (0, 0), & i = 0 \\ (\pm 1, 0)c, (0, \pm 1)c, & i = 1-4 \\ (\pm 1, \pm 1)c, & i = 5-8 \end{cases} \quad (3)$$

where $c = \delta_x / \delta_t$ is the lattice speed, with δ_x being the lattice spacing and δ_t being the time spacing. δ_x and δ_t are usually taken as 1.0 in LBM. For D3Q19 lattice, the weighting coefficients ω_i are given by $\omega_i = 1/3$ for $i = 0$; $\omega_i = 1/18$ for $i = 1-6$ and $\omega_i = 1/36$ for $i = 7-18$. The discrete velocity vectors are given as

$$\mathbf{e}_i = \begin{cases} (0, 0, 0), & i = 0 \\ (\pm 1, 0, 0)c, (0, \pm 1, 0)c, (0, 0, \pm 1)c, & i = 1-6 \\ (\pm 1, \pm 1, 0)c, (\pm 1, 0, \pm 1)c, (0, \pm 1, \pm 1)c, & i = 7-18 \end{cases} \quad (4)$$

Note that $c_s^2 = c^2/3$ in D2Q9 and D3Q19 schemes. The kinematic viscosity is determined by the relaxation time through

$$\nu = c_s^2 \left(\tau - \frac{1}{2} \right) \delta_t \quad (5)$$

The density and velocity of the fluid can be obtained by

$$\rho = \sum_i f_i \quad \rho \mathbf{u} = \sum_i \mathbf{e}_i f_i \quad (6)$$

Thus, the Navier–Stokes equations can be recovered through the Chapman–Enskog expansion procedure.

2.2. Schemes for interparticle interaction forces

As mentioned above, the interparticle interaction force accounts for the phase transition in the pseudo-potential model. In the following, we will first review two existing schemes for interparticle interaction forces and then propose a new scheme.

2.2.1. Existing schemes for interparticle interaction forces

In S–C model [4] and Yuan and Schaefer model [9], the interparticle interaction force is given by

$$\mathbf{F}_{\text{int}}(\mathbf{x}) = -c_0 \psi(\mathbf{x}) g \nabla \psi(\mathbf{x}) \quad (7)$$

where $\psi(\mathbf{x})$ is the “effective mass” which is a function of the local density, g is the interparticle interaction strength and c_0 is determined by the lattice structure. For D2Q9 and D3Q19 lattice, $c_0 = 6.0$. The equation of state of the fluid corresponding to Eq. (7) is given as

$$p = \rho c_s^2 + \frac{c_0}{2} g [\psi(\rho)]^2 \quad (8)$$

which can be rewritten as

$$\psi(\rho) = \sqrt{\frac{2(p - \rho c_s^2)}{c_0 g}} \quad (9)$$

Solving pressure p from a given equation of state, and substituting p into Eq. (9) gives the corresponding “effective mass”. Thus an arbitrary equation of state can easily be incorporated into the interparticle interaction scheme through Eq. (7). Hence, different equations of state would give different interparticle interaction force terms.

For numerical implementation, Eq. (7) is discretized as,

$$\mathbf{F}_{\text{int}}(\mathbf{x}) = -\psi(\mathbf{x}) \sum_{\mathbf{x}'} G(\mathbf{x}, \mathbf{x}') \psi(\mathbf{x}') (\mathbf{x}' - \mathbf{x}) \quad (10)$$

with $G(\mathbf{x}, \mathbf{x}')$ being Green function which satisfies $G(\mathbf{x}, \mathbf{x}') = G(\mathbf{x}', \mathbf{x})$. It reflects the interaction strength between neighboring fluid particles. A negative value of $G(\mathbf{x}, \mathbf{x}')$ means attractive force, which separates the fluid system into two phases (the liquid phase and the vapor phase) with different densities. The choice of $G(\mathbf{x}, \mathbf{x}')$ is flexible [19–21].

On the other hand, Zhang and Chen [10] proposed a straightforward way to incorporate an arbitrary equation of state. In their model, the force is written as follows

$$\mathbf{F}_{\text{int}}(\mathbf{x}) = -\nabla U = -\nabla(p - \rho c_s^2) \quad (11)$$

where $U = p - \rho c_s^2$. An arbitrary equation of state can be incorporated by substituting p from the equation of state directly to Eq. (11). Zeng et al. [11] also used this form of force term scheme in their model. For numerical implementation, Eq. (11) is discretized as

$$\mathbf{F}_{\text{int}}(\mathbf{x}) = -\frac{1}{c_0} \sum_{\mathbf{x}'} \frac{G(\mathbf{x}, \mathbf{x}')}{g} U(\mathbf{x}')(\mathbf{x}' - \mathbf{x}) \quad (12)$$

2.2.2. Proposed new scheme for interparticle interaction force

We now modify S-C's interparticle interaction force term scheme and propose a new scheme for this force term. Note that the S-C's interparticle interaction force term scheme given by Eq. (7) can be rewritten as:

$$\mathbf{F}_{\text{int}}(\mathbf{x}) = -c_0 g \nabla \psi^2(\mathbf{x})/2 \quad (13)$$

which can be discretized as.

$$\mathbf{F}_{\text{int}}(\mathbf{x}) = -\frac{1}{2} \sum_{\mathbf{x}'} G(\mathbf{x}, \mathbf{x}') \psi^2(\mathbf{x}')(\mathbf{x}' - \mathbf{x}) \quad (14)$$

Comparing Eqs. (10) and (14), it can be seen that the numerical implementations of Eqs. (7) and (13) are obviously different. While Eq. (14) involves only “effective mass” of the neighboring lattices, Eq. (10) involves the “effective mass” not only the neighboring lattices but also the local lattice as well.

We now propose a new scheme for the interparticle interaction force term by combining Eqs. (7) and (13) to give:

$$\mathbf{F}_{\text{int}}(\mathbf{x}) = -\beta c_0 \psi(\mathbf{x}) g \nabla \psi(\mathbf{x}) - (1 - \beta) c_0 g \nabla \psi^2(\mathbf{x})/2 \quad (15)$$

where β is the weighting factor depending on the particular equation of state chosen as will be discussed later in Section 3.2.1. Eq. (15) can be discretized as

$$\begin{aligned} \mathbf{F}_{\text{int}}(\mathbf{x}) = & -\beta \psi(\mathbf{x}) \sum_{\mathbf{x}'} G(\mathbf{x}, \mathbf{x}') \psi(\mathbf{x}')(\mathbf{x}' - \mathbf{x}) - \frac{1 - \beta}{2} \\ & \times \sum_{\mathbf{x}'} G(\mathbf{x}, \mathbf{x}') \psi^2(\mathbf{x}')(\mathbf{x}' - \mathbf{x}) \end{aligned} \quad (16)$$

According to our experience in modeling the droplet shape, we found that the following form [19,20] for $G(\mathbf{x}, \mathbf{x}')$ gives better results with higher isotropy so that the droplet shape appears to be more smooth,

$$G(\mathbf{x}, \mathbf{x}') = \begin{cases} g_1, & |\mathbf{x} - \mathbf{x}'| = 1 \\ g_2, & |\mathbf{x} - \mathbf{x}'| = \sqrt{2} \\ 0, & \text{otherwise} \end{cases} \quad (17)$$

where $g_1 = 2g$, $g_2 = g/2$ for D2Q9 scheme and $g_1 = g$, $g_2 = g/2$ for D3Q19 scheme. As shown in Eq. (17), only interactions between nearest and next-nearest lattices are involved in the computation.

2.3. Methods of incorporating the force term

Many fluid flow problems are subjected to external forces such as gravity and electric forces or internal forces such as interparticle interaction forces $\mathbf{F}_{\text{int}}(\mathbf{x})$ in multiphase/multicomponent flows. These forces must be treated properly in order to recover the correct hydrodynamic equations.

Methods of incorporating the force terms in LBM have attracted considerable attention in the past two decades [4,12–16] because of their important effects on the accuracy of the model. Generally speaking, the force incorporation methods can be divided into three categories: the velocity shifting method [4], the discrete force method [13–16] and the exact difference method [12]. These methods will be briefly described below.

2.3.1. Velocity shifting method

The velocity shifting method was first proposed by Shan and Chen [4]. In this method, the incorporation of the force term is realized by shifting the velocity \mathbf{u} when calculating the equilibrium distribution function, i.e., the velocity \mathbf{u} in Eq. (2) is replaced by \mathbf{u}^{eq} , which is given by

$$\mathbf{u}^{eq} = \mathbf{u} + \frac{\tau \mathbf{F}}{\rho} \delta t \quad (18)$$

where \mathbf{F} is the body force (such as $\mathbf{F}_{\text{int}}(\mathbf{x})$ mentioned above). Thus, the whole fluid velocity should be redefined by averaging the momentum before and after the collision as [22]

$$\rho \mathbf{U} = \rho \mathbf{u} + \frac{\delta t}{2} \mathbf{F} \quad (19)$$

The S-C model [4] as well as the Yuan and Schaefer model [9] used this force incorporation method.

2.3.2. Discrete force method

In the discrete force method, the discrete form of the force is added directly to the right-hand side of the evolution equation for particle distribution function given by Eq. (1). The force term is given as

$$\Delta f_i(\mathbf{x}, t) = \mathbf{F}_i(\mathbf{x}, t) \cdot \delta t \quad (20)$$

with $\mathbf{F}_i(\mathbf{x}, t)$ being the discrete form of the force. Several methods were proposed by different groups [13–16]. In Zhang and Chen model [10], the following method was used [15]

$$\mathbf{F}_i(\mathbf{x}, t) = \omega_i \frac{\mathbf{e}_i \cdot \mathbf{F}}{c_s^2} \quad (21)$$

In this method, the fluid velocity and the equilibrium distribution function are given by Eqs. (6) and (2). This discrete form is derived from Lattice Gas Automata (LGA) [23], so we will refer to it as the LGA method. Considering the discrete lattice effect and the contribution of the body force to the momentum flux, Guo et al. [16] proposed another method in 2002. Their theoretical analysis and numerical results showed that this method yielded better results than other discrete force methods. In Guo et al.'s method [16], the discrete form of the body force is given as

$$\mathbf{F}_i(\mathbf{x}, t) = \left(1 - \frac{1}{2\tau}\right) \omega_i \left[\frac{\mathbf{e}_i \cdot \mathbf{U}}{c_s^2} + \frac{(\mathbf{e}_i \cdot \mathbf{U})}{c_s^4} \mathbf{e}_i \right] \cdot \mathbf{F} \quad (22)$$

with \mathbf{U} being the whole fluid velocity which is also given by Eq. (19). Furthermore, in Guo et al.'s method, the velocity \mathbf{u} in Eq. (2) used to calculate the equilibrium distribution function should also be replaced by \mathbf{u}^{eq} , which is given by

$$\rho \mathbf{u}^{eq} = \sum_i \mathbf{e}_i f_i + \frac{\delta t}{2} \mathbf{F} \quad (23)$$

Comparing Eqs. (19), (22), and (23), it can be shown that \mathbf{u}^{eq} is equal to the whole fluid velocity \mathbf{U} in Guo et al.'s method.

2.3.3. Exact difference method

The exact difference method (EDM) was proposed by Kupershokh and Medvedev [12] to incorporate electric forces in LBM. In this method, the body force term is also added directly to the right-hand side of Eq. (1). However, it is not necessary to discretize the body force. The force term is simply given by

$$\Delta f_i(\mathbf{x}, t) = f_i^{eq}(\rho(\mathbf{x}, t), \mathbf{u} + \Delta \mathbf{u}) - f_i^{eq}(\rho(\mathbf{x}, t), \mathbf{u}) \quad (24)$$

with $\Delta \mathbf{u} = \mathbf{F} \cdot \delta t / \rho$ being the velocity change due to the body force during time step δt . Note that the whole fluid velocity is also given by Eq. (19). This method will be adopted to incorporate the interparticle interaction force in our model due to its better

accuracy and convenience to implement as will be discussed in Section 3.2.2.

3. Performances of the proposed model

In this section, we will first give a brief introduction to the theory of Maxwell construction for non-ideal equations of state and obtain the so-call coexistence curves in Section 3.1 for comparison purposes. The performances of different interparticle interaction force schemes and force incorporation methods with respect to accuracy and stability will be compared in Sections 3.2.1 and 3.2.2, respectively. Combining the force scheme and force incorporation method together, we will investigate performances of our proposed model with other existing models in terms of accuracy, applicable temperature range and spurious currents in Section 3.2.3.

Three most popular equations of state for non-ideal gases are considered in this paper, and they will be briefly discussed below:

(i) The Shan and Chen (S-C) equation of state:

$$p = \frac{1}{3}\rho + \frac{c_0}{2}g\rho_0^2[1 - \exp(-\rho/\rho_0)]^2 \quad (25)$$

The above equation of state was first proposed by Shan and Chen [4], where ρ_0 was chosen to be 1.0. Setting the first and second derivatives of pressure given by Eq. (25) with respect to density to zero, we can obtain the critical point for the S-C equation of state. For S-C equation of state given by Eq. (25), the critical properties are:

$$\rho_c = \rho_0 \ln 2 \quad (26a)$$

$$g_c = -\frac{2}{9\rho_0} \quad (26b)$$

with the subscript c denoting the critical condition. Unlike other equation of state, there is no temperature parameter T in S-C equation of state. So the temperature is defined as $T = -1/g$. It follows from Eq. (26b) that the critical temperature is $T_c = 4.5\rho_0$.

(i) The van der Waals (vdW) equation of state is given by,

$$p = \frac{\rho RT}{1 - b\rho} - a\rho^2 \quad \text{or} \quad \left(p + \frac{a}{V^2}\right)(V - b) = RT \quad (27)$$

which was proposed in 1873. Eq. (27) is the most well-known equation of state for real gases. In the above equation, a is the attraction parameter accounting for attractive forces between molecules, and b is the repulsion parameter accounting for the non-negligible volume of molecules. The critical properties for vdW equation of state are: $\rho_c = 1/(3b)$, $p_c = a/(27b^2)$, $T_c = 8a/(27Rb)$. Setting $a = 9/49$, $b = 2/21$ and $R = 1$ arbitrarily, we get $\rho_c = 3.5$ and $T_c = 4/7$.

(i) The Peng–Robinson (P-R) equation of state is given by

$$p = \frac{\rho RT}{1 - b\rho} - \frac{a\rho^2\alpha(T)}{1 + 2b\rho - b^2\rho^2} \quad (28)$$

where $\alpha(T) = [1 + (0.37464 + 1.54226\omega - 0.26992\omega^2)(1 - \sqrt{T/T_c})]^2$, with ω being the acentric factor which is determined by the substance under consideration. The critical properties can be obtained by: $a = 0.45724R^2T_c^2/p_c$, $b = 0.0778RT_c/p_c$. ω is chosen as 0.344 in this paper, which is the acentric factor of water. For P-R equation of state, we set $a = 2/49$, $b = 2/21$ and $R = 1$ arbitrarily. Although the P-R equation of state has a slightly more complex form than that of vdW equation of state, it is a much more accurate equation of state, especially for water and ammonia.

3.1. Maxwell construction of p - v curves for non-ideal equations of state

Fig. 1 is a sketch showing the p - v curve of a pure substance at a given temperature for any of the non-ideal equation of state given by Eqs. (25), (27) or (28). If the substance is supercritical, i.e., $T > T_c$ (with T_c being the critical temperature), the p - v curve at constant temperature is monotonic and each value of pressure corresponds to a single specific volume/density. In this situation, no distinct vapor and liquid phases can be distinguished. On the other hand, if the temperature of the substance is subcritical, i.e., $T < T_c$, the curve for the equation of state is no longer monotonic and this allows the coexistence of different densities/specific volumes of the substance at a single pressure, meaning that separation of the liquid phase and vapor phase occurs (i.e., in the saturated mixture regime, with saturated liquid and saturated vapor in equilibrium). Densities (or specific volumes) of the saturated vapor and the saturated liquid at a given temperature T can be determined by the Maxwell construction, in which the unphysical oscillatory part 1-4-3-5-2 is replaced by a horizontal line 1-3-2. The basic idea of Maxwell construction is

$$\int_{v_l}^{v_g} p dv = p_s(v_g - v_l) \quad (29)$$

Eq. (29) is equivalent to specify area A equal to area B in Fig. 1. For the numerical solution of Eq. (29) for a given equation of state at a given temperature, the first step is solving p from the equation of state and substituting it into Eq. (29) with assumed values of v_l , v_g and p_s . The final values of v_l , v_g and p_s are obtained iteratively until Eq. (29) is satisfied. The values of reduced temperature T_r versus the reduced specific volume v_r (defined by $v_r = 1/\rho_r = \rho_c/\rho$, $T_r = T/T_c$) for three non-ideal equations of state given by Eqs. (25), (27), and (28), i.e., S-C, vdW and the P-R are presented as solid curves in Figs. 2–4, which have been called “coexistence curves” in the literature [9]. Note that in the coexistence curves presented in Figs. 2–4, $v_r = 1$ at $T_r = 1$ is at the critical state. Thus, $v_r < 1$ denotes the saturated liquid branch and $v_r > 1$ denotes the saturated vapor branch.

3.2. Comparisons of simulation results with those from Maxwell construction

Consider simulating the formation of a liquid droplet in a vapor of an infinite extent which was considered previously by Yuan and Schaefer [9]. At a given temperature T , initial density distribution at the central domain with an arbitrary radius (say $r = 20$) is set slightly higher than the critical density ρ_c and lower than ρ_c

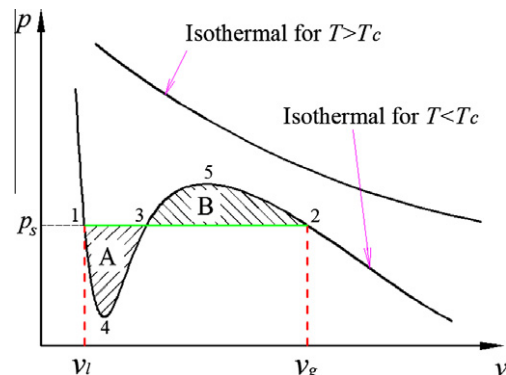


Fig. 1. Schematic illustrations of the supercritical, subcritical behaviors and Maxwell construction (v_l and v_g denote the specific volume of the saturated liquid and saturated vapor, respectively. p_s denote the saturated pressure corresponding to temperature T).

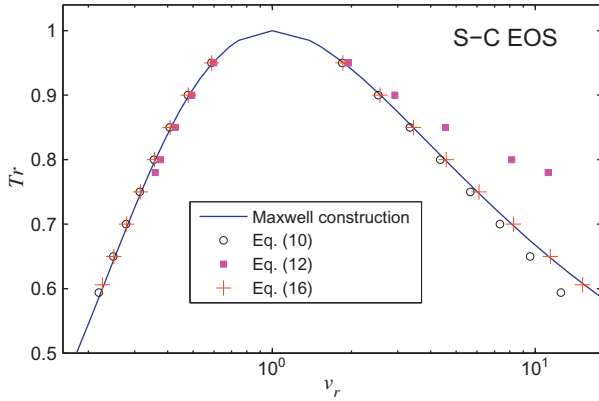


Fig. 2. Coexistence curves of S-C equation of state ($\tau = 1.0$) for different schemes of interparticle interaction force term with the same velocity shifting method.

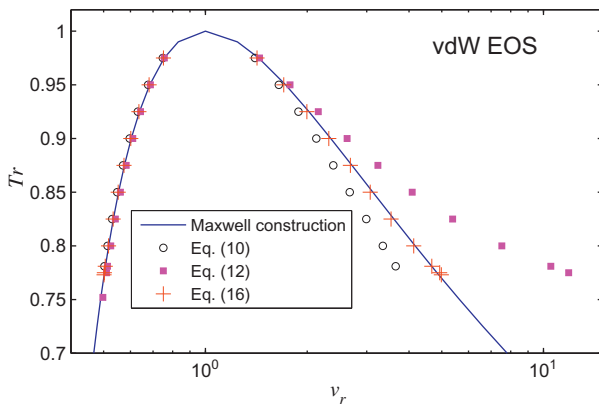


Fig. 3. Coexistence curves of vdW equation of state ($\tau = 1.0$) for different schemes of interparticle interaction force term with the same velocity shifting method.

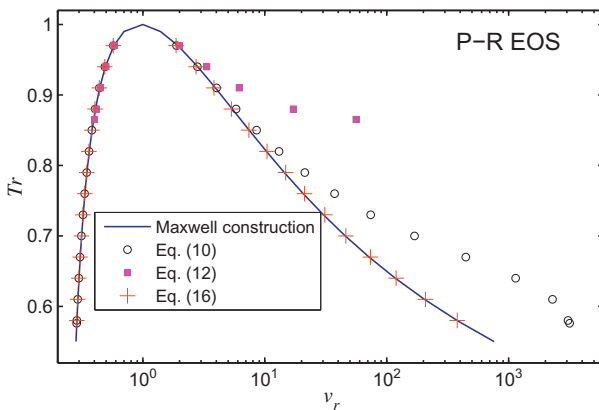


Fig. 4. Coexistence curves of P-R equation of state ($\tau = 1.0$) for different schemes of interparticle interaction force term with the same velocity shifting method.

elsewhere. Periodic boundary conditions are imposed on all directions to simulate an infinite domain. To save time and ensure accuracy, an 81×81 lattice structure was chosen for computation. Using multiphase LBM with different schemes for interparticle interaction force terms and different methods of incorporating the force term as discussed in Section 2, each computation run was carried out for 40,000 time steps to ensure that the steady state was reached. At the steady state, a liquid droplet (with specific volume v_l) surrounded by the vapor (with specific volume

v_g) was formed in the central domain. Simulation results of v_l and v_g will be compared with those results based on Maxwell construction obtained from Section 3.1.

3.2.1. Comparison of different interparticle interaction forces and determination of weighting factor β

We now compare performances (in terms of accuracy and temperature range) of three schemes of interparticle interaction force given by Eqs. (10), (12), and (16) with respect to equations of state given by S-C, vdW and P-R, respectively. The velocity shifting method will be used for incorporating three different force term schemes. The weighting factor β in Eq. (16) for three non-ideal equations of state will be determined by matching the simulation results with those from Maxwell construction.

LBM simulation results with three different schemes of interparticle interaction force term given by Eqs. (10), (12), and (16) are presented in Fig. 2 with those from Maxwell construction for non-ideal gases. As shown from this figure, all three schemes yield relatively satisfactory results at high temperatures (i.e., $T_r \approx 1$). However, as the temperature is reduced (i.e., for smaller T_r), simulation results of Eqs. (10) and (12) begin to deviate from those obtained based on Maxwell construction, especially on the vapor branch (where $\rho < \rho_c$ or $v_r > 1$). The proposed scheme for interparticle interaction force term given by Eq. (16) with $\beta = 0.886$ gives the most accurate results at low temperatures for S-C equation of state. As a matter of fact, densities predicted by Eqs. (10), (12), (16) are within $\pm 34.6\%$, $\pm 54.7\%$, $\pm 1.6\%$ of those based on Maxwell construction respectively. It can be seen from Fig. 2 that for S-C equation of state, the lowest temperature that Eq. (12) can give stable results is $0.78 T_c$. On the other hand, Eqs. (10) and (16) can give stable results in a much wider temperature range with the lowest temperature about $0.6 T_c$.

Note that in the above LBM simulations, all the variables are represented by lattice unit. To relate them to real physical properties, the principal of reduced properties are used, i.e., the reduced properties in lattice unit are equal to that in real unit. As mentioned above, the reduced density is given by $\rho_r = \rho / \rho_c$. So we can get $\rho^{Lu} / \rho_c^{Lu} = \rho^{real} / \rho_c^{real}$, which gives $\rho^{real} = \rho_c^{real} \rho^{Lu} / \rho_c^{Lu}$, where the superscripts *Lu* and *real* denote the lattice unit and real unit, respectively.

Coexistence curves for vdW equation of state with different schemes for interparticle interaction force term are presented in Fig. 3. It is shown that only the proposed scheme for interparticle interaction force term, given by Eq. (16) with $\beta = 0.550$, gives accurate results even at low temperatures. Densities predicted by the three different schemes given by Eqs. (10), (12), (16) are within $\pm 27.8\%$, $\pm 74.8\%$, $\pm 1.9\%$ of analytical solutions, respectively. We can also see that Eq. (12) give stable results in a slightly wider temperature range than those of Eqs. (10) and (16), which is different from Fig. 2.

Coexistence curves for P-R equation of state with different schemes for interparticle interaction force term are presented in Fig. 4. As shown, simulation results given by Eqs. (10) and (12) deviate from Maxwell construction results drastically at low temperatures. The proposed scheme for interparticle interaction force term, given by Eq. (16) with $\beta = 1.16$, can give stable results in a wide temperature range with accurate results even at low temperatures. Table 1 summarizes the weighting factors β for three non ideal equations of state.

Table 1
Weighting factors β for three equations of state.

Equation of state	S-C	vdW	P-R
Weighting factor β	0.886	0.55	1.16

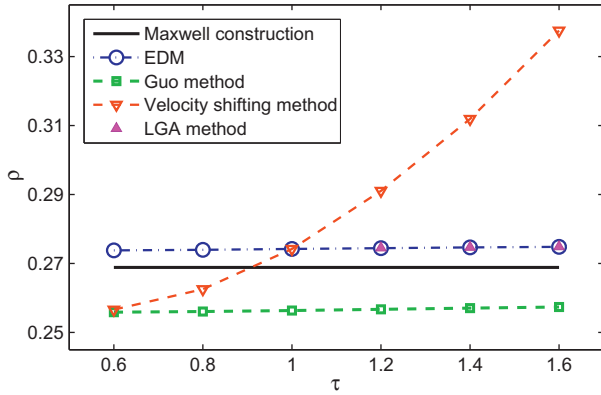


Fig. 5. Comparison of LBM simulation results for S-C force term with different force incorporation methods.

3.2.2. Comparison of different force incorporation methods on relaxation times

In this section, we investigate performances (in terms of accuracy, stability and the dependency of relaxation time) of the three force incorporation methods: the velocity shifting method [4], discrete force method (including Guo et al.'s method [16] and LGA method [15]), and the exact difference method [12].

A comparison of densities of the saturated vapor at $T_r = 0.9$ versus relaxation times, computed based on the same force term scheme given by Eq. (10) but with four different force incorporation methods, are presented in Fig. 5 where the solid horizontal line is obtained from the Maxwell construction given by Eq. (25). As can be seen from Fig. 5, LGA method suffers from poor stability and stable numerical results can only be obtained in a narrow range of relaxation time τ ($\tau > 1.0$). It is relevant to point out that densities of the saturated vapor and saturated liquid should depend only on temperature for any given equation of state. Fig. 5 shows that the densities of the saturated vapor, computed based on velocity shifting method, depend on relaxation time which is physically unrealistic. This is because the velocity shifting method is not a good method for incorporation of the force term. Both Guo et al.'s method [16] and the exact difference method (EDM) [12] give stable numerical results in a wide range of τ , and avoid the physically unrealistic phenomenon of relaxation time dependence. However, EDM has better accuracy (closer to the results given by Maxwell construction as can be seen from Fig. 5) than Guo et al.'s method and is also easier to implement.

3.2.3. Comparison of proposed model with existing models

As shown in Section 3.2.1, the results from the LBM simulation with the new scheme for the force term, given by Eq. (16) with β from Table 1, are more accurate than with other force term schemes. Furthermore, it is shown in Section 3.2.2 that if the exact difference method (EDM) is used for incorporating the force term in the LBM simulations, it will give numerical results independent of the relaxation times. It follows that it is desirable to construct a model consisting of the above two features in the LBM for the simulation of multiphase flows. This is our proposed improved model of multiphase LBM for the simulation of multiphase flows. In the following, we will compare the performances (in terms of accuracy, applicable temperature range and spurious currents) of the proposed improved model with other existing models for simulation of droplet formation in a vapor of infinite extent as discussed in Section 3.2.

Fig. 6 shows the comparison of coexistence curves simulated by the proposed improved model and those from other existing models by Yuan and Schaefer [9], Zhang and Chen [10], Zeng et al. [11]

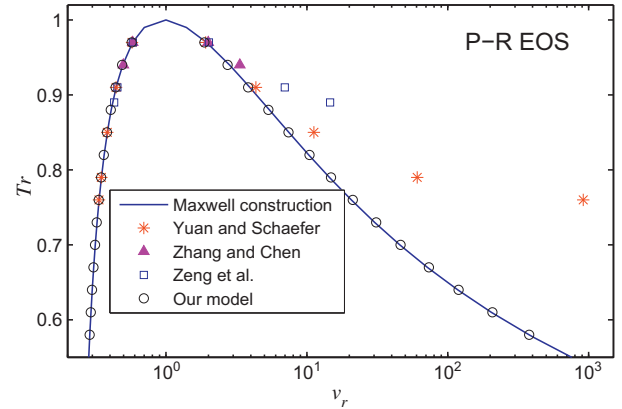


Fig. 6. Coexistence curves ($\tau = 0.9$) based on P-R equation of state.

based on P-R equation of state. It is seen that the proposed model not only gives much more accurate results than other existing models, but also greatly enlarges the temperature range where stable numerical results can be obtained. As shown in Fig. 6, stable numerical results from the proposed model with P-R equation of state can be obtained for a density ratio as high as 1300 at a low temperature of $T_r = 0.58$.

It is known that spurious currents represent the unphysical velocities generated in simulations. It was pointed out by Yuan and Schaefer [9] that large spurious currents can make the simulation unstable and reduce the accuracy of the velocity field. Although it is impossible to avoid spurious currents in LBM simulations for multiphase flows, spurious currents can be reduced. Since the models of Zhang and Chen [10] as well as Zeng et al. [11] give stable solutions in a very limited temperature range, so we only need to compare spurious currents in Yuan-Schaefer model [9] and the proposed model. For the problem of liquid droplet formation in a vapor of infinite extent, velocity should be zero everywhere at the steady state. Thus, the maximum velocity $|u|_{\max}$ at the steady state obtained from the LBM simulation for this problem can be chosen as a measure of the spurious currents. The results of such computations are presented in Fig. 7. It is shown that when $T_r < 0.8$, spurious currents increase drastically in Yuan-Schaefer model [9] while the increase of spurious currents at small T_r in the proposed model is relatively smooth and small. This may explain why the proposed model can give stable results in a much wider temperature range than other existing models [9].

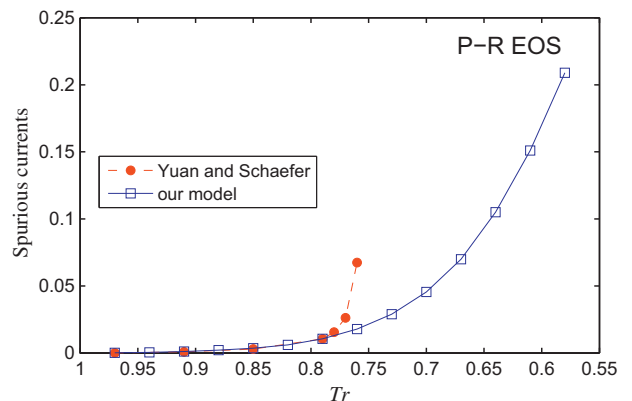


Fig. 7. Comparison of spurious currents ($|u|_{\max}/c_s$) vs. T_r obtained from Yuan and Schaefer's model and the proposed model ($\tau = 0.9$).

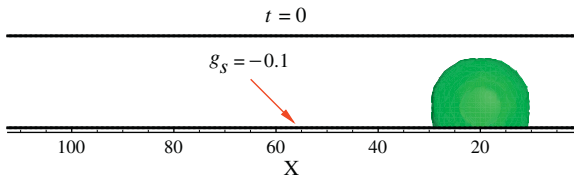


Fig. 8. Placement of a droplet on x - z plane with center at $y = 20$ ($x = 20$) at initial state.

4. Simulations of 3D droplet movements by our proposed model

Manipulations of droplets have received a great deal of attention in recent years due to their wide engineering applications [7,8,25–30]. Using the VOF method to track the interface, Nikolopoulos et al. [7] investigated central binary collision of droplets numerically. Lee and Son [8] studied the droplet impact and coalescence processes on a substrate by level set method. Manservigi and Scardovelli [27] investigated the contact angle dynamics of spreading droplets by a finite element model coupled with an interface front-tracking method. Gupta and Kumar studied droplet impingement at low density ratio [29] and high density ratio (coauthoring with Gu) [30].

In this section, we investigate the droplet motion and coalescence processes driven by wettability gradients on solid surfaces based on our proposed lattice Boltzmann model, i.e., (i) using Eq. (16) as the interparticle interaction force scheme, and (ii) the EDM for incorporating the force term. Note that the computation cost of our model is lower than the aboved mentioned macroscopic models [7,8,27] due to the fact that there is no need to track the interface. The wettability (contact angle) of the solid wall can be conveniently implemented by introducing interaction force between the solid and the fluid [24]. For D3Q19 scheme, this force can be written as [18]

$$\mathbf{F}_s(\mathbf{x}) = -\psi(\mathbf{x}) \sum_i 18g_s \omega_i s(\mathbf{x} + \mathbf{e}_i \delta_t) \cdot \mathbf{e}_i \delta_t \quad (30)$$

where g_s is the fluid–solid interaction strength for controlling the wetting conditions (contact angles). Indicator function $s(\mathbf{x})$ is equal to 1 when \mathbf{x} is in solid, and is equal to 0 when \mathbf{x} is in fluid. Under this situation, the body force \mathbf{F} in Eqs. (18)–(24) is given by

$$\mathbf{F} = \mathbf{F}_{\text{int}}(\mathbf{x}) + \mathbf{F}_s(\mathbf{x}) \quad (31)$$

The following two problems are studied numerically by the proposed improved multiphase LBM method.

4.1. Droplet movement and deformation driven by wettability gradients

It is known that facilitating discharge of liquid droplets emerging from the diffusion layer into a gas channel can avoid water flooding problems in a PEM fuel cell. Using the free energy lattice Boltzmann method, Hao and Cheng [25] studied liquid droplet movement driven by a shear flow along a uniform hydrophobic wall of the gas channel. Due to the limitation of the model they used, density ratio of liquid to gas phase was chosen to be 1:1.

We now apply the proposed model to simulate movement and deformation of a droplet on the bottom surface with different wettability gradients in a microchannel. For this purpose, a $121 \times 41 \times 21$ lattice structure was chosen to be the computational domain. Initially ($t = 0$), a liquid droplet having a radius $r = 10$ with its center at $(20, 20, 5)$ is placed in contact with the bottom surface at $z = 0$ where the fluid–solid interaction strength g_s is set to be uniform at -0.1 (corresponding to a static contact angle of 145°) as shown in Fig. 8. In order to identify the position of the interface, we define a critical density $\rho_{\text{crit}} = (\rho_l + \rho_g)/2$, where ρ_l and ρ_g are densities of the liquid phase and vapor phase, respectively. The lattice nodes with density higher than ρ_{crit} are assigned to be liquid nodes. Computations were carried out for S–C equation of state with $T_r = 0.65$ corresponding to a liquid/vapor density ratio about 45 (see Fig. 2). From Eqs. (9) and (25), we obtain the effective mass $\psi(\rho) = \rho_0[1 - \exp(-\rho/\rho_0)]$, where ρ_0 was chosen to be 1.0. Relaxation time τ was also chosen as 1.0. Periodic boundary conditions are imposed on x and y directions, and the half-way bounce back scheme which has an accuracy of two order is imposed on the top ($z = 20$) and bottom ($z = 0$) walls of the microchannel.

As the first step, the proposed model of multiphase LBM was used for numerical simulation of formation of the stationary droplet beginning from $t = 0$ until an equilibrium state is reached at $t = 10,000$. At this equilibrium state, the droplet at $x = 20$ becomes a truncated sphere in shape as shown in left-hand side of Fig. 9 on a

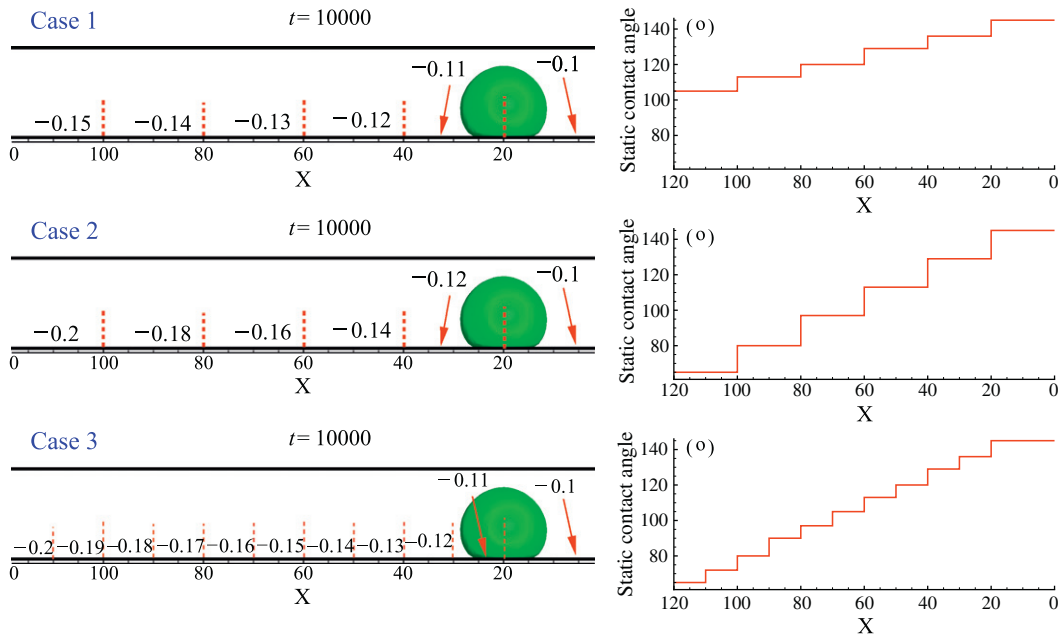


Fig. 9. Surface with three different wettability gradients (x - z plane, $y = 20$).

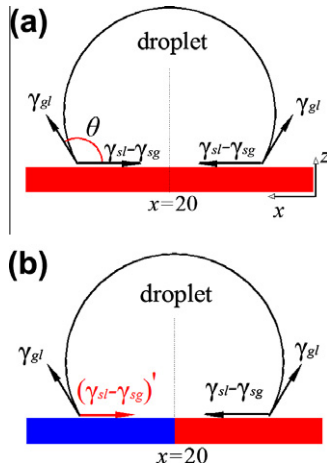


Fig. 10. Schematic of the force analysis at $t = 10,000$ (x - z plane, $y = 20$): (a) $t = 10,000^-$, (b) $t = 10,000^+$.

surface with a uniform contact angle of 145° (corresponding to a hydrophobic surface with $g_s = -0.1$).

Beginning at this moment ($t = 10,000^+$), wettabilities of the bottom surface of the microchannel are suddenly changed as follows:

- (i) **Case 1:** g_s is stepwise decreasing (with $\delta g_s = 0.01$ for every 20 lattice spaces in the x -direction) from $g_s = -0.1$ (corresponding to a static contact angle of 145° , i.e., a hydrophobic surface) at $x = 0-20$ to $g_s = -0.15$ (corresponding to a static contact angle of 105° , i.e., a hydrophobic surface) at $x = 100-120$.

- (ii) **Case 2:** g_s is stepwise decreasing (with $\delta g_s = 0.02$ for every 20 lattice spaces in the x -direction) from $g_s = -0.1$ at $x = 0-20$ to $g_s = -0.2$ (corresponding to a static contact angle of 65° , i.e., a hydrophilic surface) at $x = 100-120$.
- (iii) **Case 3:** g_s is stepwise decreasing (with $\delta g_s = 0.01$ for every 10 lattice spaces in the x -direction) from $g_s = -0.1$ at $x = 0-20$ to $g_s = -0.2$ at $x = 110-120$.

The corresponding stepwise decreasing in static contact angles from right to left hand side of the bottom surface for the three cases are shown on the right-hand side of Fig. 9. As shown (from Fig. 9), an approximately linear relationship between g_s and the static contact angle can be seen, which is consistent with literature [31]. Thus, we can evaluate the value of g_s by the static contact angle that is needed. For more details about the contact angle analysis, readers can refer to literature [32]. In order to illustrate the mechanism of the droplet movement under a wettability gradient, force analyses at $t = 10,000^-$ and $t = 10,000^+$ are shown in Fig. 10a and b, where γ_{gl} , γ_{sl} , γ_{sg} represent interfacial tension of gas-liquid, solid-liquid, and solid-gas, respectively. As shown, the droplet at $t = 10,000^-$ is at a steady state with a static contact angle of $\theta = 145^\circ$. The Young-Laplace equation gives,

$$\gamma_{sg} - \gamma_{sl} = \gamma_{gl} \cos \theta \quad (32)$$

At $t = 10,000^+$, the force $\gamma_{sl} - \gamma_{sg}$ at the left decreases to $(\gamma_{sl} - \gamma_{sg})'$ at the left-hand side of the surface. Thus, the force in x direction is no longer in balance and the droplet begins to move toward left.

The droplet subsequent movement along the bottom surface of the microchannel, driven by wettability gradients from $x = 20$ to $x = 120$, was simulated using the proposed LBM model. The simulation results for the movements of droplets on three bottom surfaces with different wettability distributions are presented in

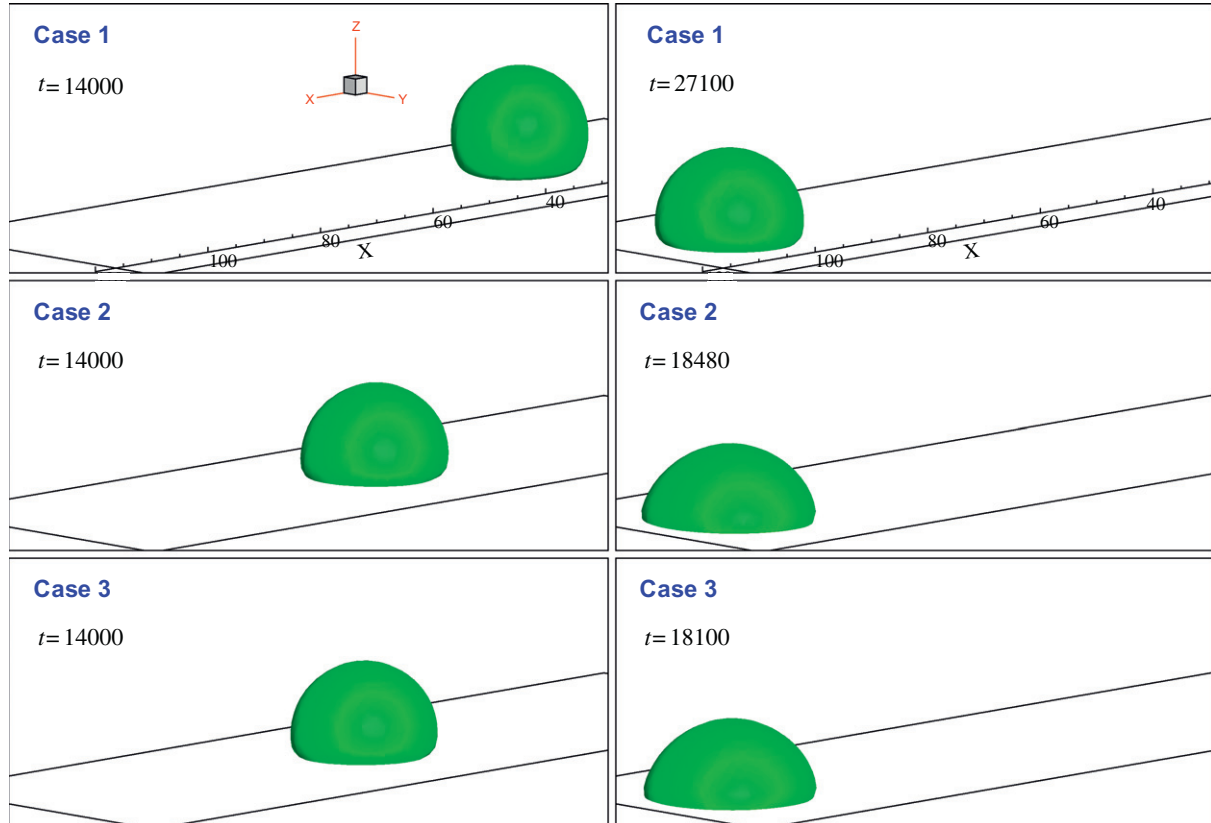


Fig. 11. Three dimensional droplet movement and deformation under wettability gradients.

Fig. 11. The left-hand side of Fig. 11 show the positions of the droplet at $t = 14,000$ on the three surfaces indicating that the droplet moves most slowly in Case 1, where the wettability gradient is smallest. The right-hand side of Fig. 11 shows that the droplet reaches the other end of the channel at $t = 27,100$, 18,480 and 18,100 for Cases 1, 2, and 3 respectively. It is shown that Cases 2 and 3 need less than half of time to reach the other end of the channel than Case 1 due to higher wettability gradients (contact angle gradient). Comparing Cases 2 and 3, we find that the droplet in Case 3 with more wettability discontinuities moves faster because the droplet is pulled each time when it passes a wettability discontinuity.

Fig. 12 shows the side view of droplet shapes and their surrounding velocity fields for Case 2 at $t = 15,060$ and $t = 16,000$, respectively. At $t = 15,060$, the front of the moving droplet has just past the position at $x = 80$ where wettability discontinuity exists. The advancing and receding angles at this instant are 87° and 96° , respectively. The small vortex (indicated by the dashed circle) near $x = 80$ is generated by the wettability discontinuity on the bottom surface. Fig. 12b is an enlarged view of the dashed circle in Fig. 12a showing clearly the vortex motion. This vortex is responsible for the droplet rolling motion. It explains why Case 3 with more wettability discontinuities (where vortices are formed) would provide more driving force to transport the droplet. It is interesting to note from Fig. 12a that four bigger vortices are induced outside the moving droplet, two of which are moving in clockwise direction and the other two are moving in counterclockwise direction.

The acceleration and speed of the moving droplet is determined by the relative strength of the driving force caused by the wettability gradient and the viscous resistance of the fluid. Fig. 12c shows the speed of the droplet (indicated by the length of the velocity vector) at $t = 16,000$ is higher than those at $t = 15,060$, indicating the droplet is undergoing acceleration. At this instant, the droplet has an advancing contact angle of 85° and a receding contact angle of 95° which differ from that shown in Fig. 12a, indicating the dynamic contact angles are changing with respect to time. The small vortex inside the droplet disappears as the front of the droplet passes the point at $x = 80$ where wettability discontinuity exists. Note that the velocity topology is quite different in region A and region B. In region A (i.e., $x > 80$) where the droplet has passed the wettability discontinuity, the vertical velocity is moving downward and its magnitude is small compared with the leftward horizontal velocity. On the other hand, in region B (i.e., $x < 80$) of the droplet, the vertical velocity is moving upward and its magnitude is comparable with the leftward horizontal velocity.

It is interesting to note that an approximately linear leftward horizontal velocity (i.e., parallel to the surface) distribution in z direction occurs in both Fig. 12a and c. This linear velocity distribution in z direction at any x and the downward vertical velocity in left part of the droplet together with the upward movement in right part of the droplet demonstrate that the droplet is undergoing a rolling motion along the bottom wall of the microchannel. Note that the velocity topology shown in Fig. 12 is much more complex than those in Ref. [25], where the droplet is driven primarily under the action of the shearing stress of the gas flow superimposed with a small rolling motion.

4.2. Droplet coalescence driven by wettability gradients

In this section, the coalescence of two droplets driven by the wettability gradient is simulated by the new LBM model. For this purpose, an $81 \times 41 \times 31$ lattice structure was adopted as the computational domain. Initially ($t = 0$), two identical droplets having a radius $r = 10$ with their centers at $(20, 20, 0)$ and $(60, 20, 0)$ are placed separately from each other, and in contact with the bottom

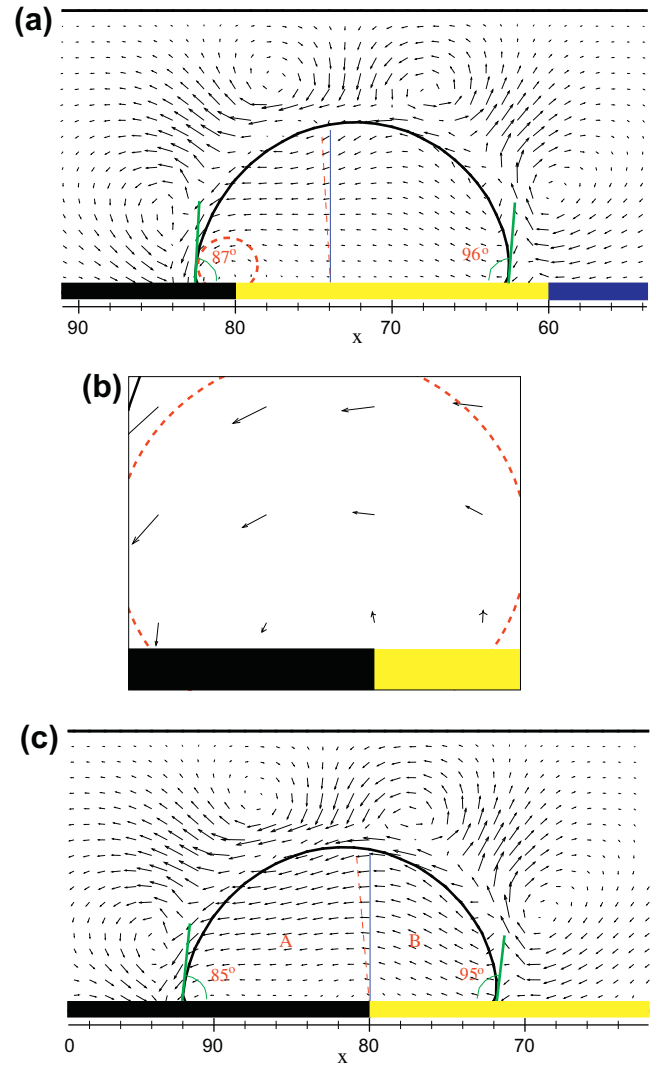


Fig. 12. Side view of the droplet shape and the surrounding velocity field for Case 2 (x - z plane, $y = 20$) at two different times: (a) $t = 15,060$, (b) Enlarged view of the dashed circle in Fig. 12a, (c) $t = 16,000$.

surface of a microchannel at $z = 0$ where the fluid–solid interaction strength g_s is set to be -0.1 as shown in Fig. 13a. Boundary conditions, density ratio and equation of state are the same as in Section 4.1. At $t = 10,000^-$, the two separate stationary droplets at $x = 20$ and 60 reach an equilibrium state on the bottom surface of the microchannel with a contact angle of 145° as shown in Fig. 13b. After this moment ($t = 10,000^+$), the wettability of the surface g_s at the middle of the bottom surface ($20 < x < 60$) is decreased to -0.15 . Thus, the two droplets, driven by wettability discontinuities at $x = 20$ and 60 , begin to move toward middle part of the surface at $x = 40$. Finally, the two droplets coalesce to form a larger droplet at the center of the bottom surface ($x = 40$) in the microchannel. This larger droplet reaches its equilibrium state with a contact angle of 105° at $t = 20,000$ as shown in Fig. 13c. In order to check the mass conservation of the droplet, we calculated the mass of the droplet at $t = 10,000$ and $t = 20,000$. The relative difference of the droplet mass at these two time steps was found to be less than 0.6% , indicating that the simulation results satisfy the mass conservation requirement.

Fig. 14a shows the three dimensional coalescence process of the two droplets driven by wettability discontinuities from $t = 10,520$ to $t = 10,820$. Fig. 14b is a top view showing the changing shapes of the droplets during the same period of time. It is interesting to

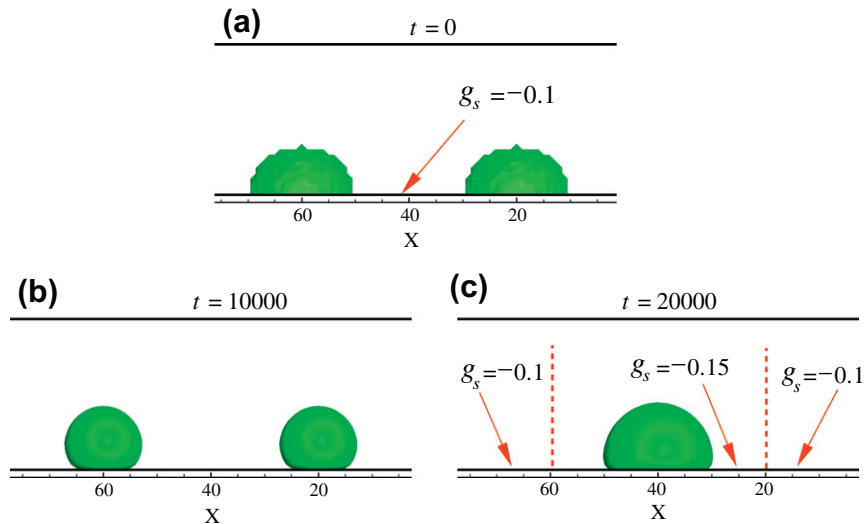


Fig. 13. Side view of the droplet(s) shape at $t = 0, 10,000, 20,000$ (x - z plane, $y = 20$).

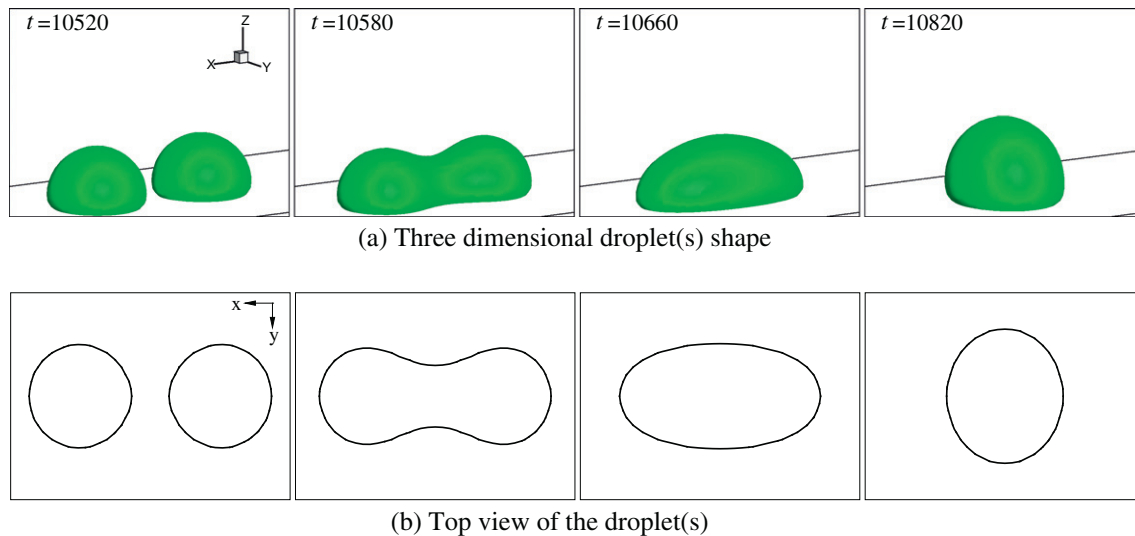


Fig. 14. Coalescence of two droplets on the bottom surface with wettability gradients in a microchannel.

note that the long axis of the droplet is in x -direction at $t = 10,660$ and in y -direction at $t = 10,820$, indicating that the shape of the droplet is experiencing an oscillation process after coalescence and before the final equilibrium state is reached. Using electrowetting to change the surface wettability, Aminfar and Mohammadpourfard [33] numerically investigated droplet splitting process under wettability gradient, which is the reversed process of droplet coalescence shown in Fig. 14 of this paper. It is found that changing shapes of the droplets in these two processes are very similar.

Fig. 15 shows the velocity fields inside and outside of the droplet(s) corresponding to the four time steps in Fig. 14. From the velocity vectors, it can be seen that the left droplet is moving toward right and the right droplet is moving toward left at $t = 10,520$. At this instant, fluid velocities between the two droplets are higher due to the squeezing effect. Four vortices can be seen above the two droplets, two of which are moving in clockwise direction and the other two are moving in counterclockwise direction. At a later time of $t = 10,580$, the two droplets coalesce to form

a larger droplet. The velocity field in the middle part of the newly formed droplet changes drastically compared with $t = 10,520$ because the coalescence first happens in this region. On the other hand, change of velocity fields at the left and right part in the droplet is not apparent because velocity fields there are still not affected by the coalescence process which is happening in the middle part of the droplet. Compared with $t = 10,520$, the middle two vortices merge and disappear due to the coalescence of the two droplets. At $t = 10,660$, velocity field at the left and right part of the droplet changes drastically, indicating that it has been affected by the coalescence process at this time. It can be seen that the velocities in the left and right parts of the droplet are moving toward the top of the droplet. Interestingly, two smaller vortices are growing around the left and right edge of the droplet near the bottom surface of the microchannel. At $t = 10,820$, the two smaller vortices on the bottom surface grow stronger and the other two vortices on the top of the droplet that disappear at $t = 10,580$ appear again. Thus, six vortices are induced by the oscillating

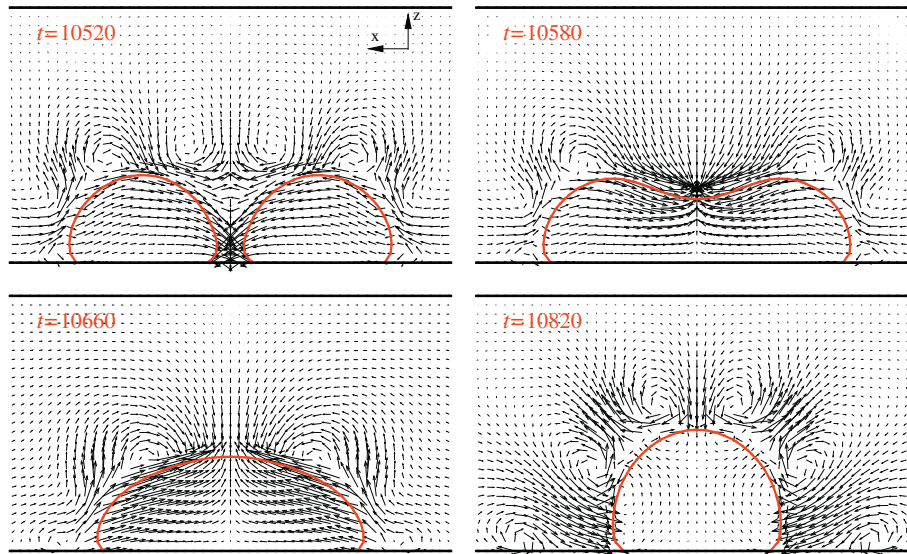


Fig. 15. Side view of the droplet(s) and the surrounding velocity field.

motion of the droplet at this time step, four of which are adjacent to the droplet and the other two are located at the bottom of the microchannel.

5. Concluding remarks

In this paper, we have studied the force term and the method of incorporating the force term individually in the single-component multiphase lattice Boltzmann method, and find that both of them play an important role in the performance for numerical simulation of multiphase flows. The results in this paper can be summarized as follows:

1. A new form of interparticle interaction force term given by Eq. (16), modified from the S–C force term, is proposed. Any equation of state can be incorporated into the proposed model. Simulation results for droplet formation based on the proposed force term with S–C equation of state, vdW equation of state and P–R equation of state in the proposed model suggest that the proposed force term can greatly improve the coexistence curves in a wide temperature range.
2. The performances of the existing force incorporation methods (including the velocity shifting method, the discrete force method and the exact difference method) are compared. Among these three methods, the exact difference method (EDM) is found to be the best due to its simplicity and accuracy. Furthermore, it avoids the unphysical phenomenon of relaxation time dependence.
3. The proposed improved model for multiphase LBM consists of (i) using a new force term given by Eq. (16), and (ii) using EDM for incorporating the force term. Compared with other existing models, the proposed model gives much accurate simulation results, and stable numerical results can be obtained in a much wider temperature range. The latter may be owing to the fact that the spurious current at small T_r is smaller in the proposed model than existing models. If the P–R equation of state is used with the proposed model, stable solutions can be obtained for a density ratio as high as 1300 at a low temperature of $T_r = 0.58$.
4. The proposed model was applied to simulate three dimensional droplet motion and coalescence processes on bottom surfaces with wettability gradients. The velocity field and

the driving mechanism for droplet motion are illustrated in details. The results of these applications suggest that our proposed model is an effective tool for simulations of phase transitions and multiphase flows and has the potential of simulating more complex fluid problems at a wider temperature range. More applications of the proposed model will be shown in a future paper.

Acknowledgment

This work was supported by National Natural Science Foundation of China through Grant No. 51036005.

References

- [1] Cheng P, Wu H. Mesoscale and microscale phase-change heat transfer. *Adv Heat Transfer* 2006;39:461–563.
- [2] Wu H, Cheng P. Boiling instability in parallel silicon microchannels at different heat flux. *Int J Heat Mass Transfer* 2004;47:3631–41.
- [3] Quan X, Cheng P, Wu H. Transition from annular flow to plug/slug flow in condensation of steam in microchannels. *Int J Heat Mass Transfer* 2008;51:707–16.
- [4] Shan X, Chen H. Lattice Boltzmann model for simulating flows with multiple phases and components. *Phys Rev E* 1993;47:1815–9.
- [5] Swift MR, Osborn WR, Yeomans JM. Lattice Boltzmann simulation of nonideal fluids. *Phys Rev Lett* 1995;75:830–3.
- [6] Gunstensen AK, Rothman DH, Zaleski S, Zanetti G. Lattice Boltzmann model of immiscible fluids. *Phys Rev A* 1991;43:4320–7.
- [7] Nikolopoulos N, Nikas KS, Bergeles G. A numerical investigation of central binary collision of droplets. *Comput Fluids* 2009;38(6):1191–202.
- [8] Lee W, Son G. Numerical study of droplet impact and coalescence in a microline patterning process. *Comput Fluids* 2011;42(1):26–36.
- [9] Yuan P, Schaefer L. Equations of state in a lattice Boltzmann model. *Phys Fluids* 2006;18:042101.
- [10] Zhang R, Chen H. Lattice Boltzmann method for simulations of liquid–vapor thermal flows. *Phys Rev E* 2003;67:066711.
- [11] Zeng J, Li L, Liao Q, Cui W, Chen Q, Pan L. Simulation of phase transition process using lattice Boltzmann method. *Chinese Sci Bull* 2009;54:4596–603.
- [12] Kupershtokh AL, Medvedev DA. Lattice Boltzmann equation method in electrohydrodynamic problems. *J Electrostat* 2006;64:581–5.
- [13] Martys NS, Shan X, Chen H. Evaluation of the external force term in the discrete Boltzmann equation. *Phys Rev E* 1998;58:6855–7.
- [14] He X, Shan X, Doolen GD. Discrete Boltzmann equation model for nonideal gases. *Phys Rev E* 1998;57:R13–6.
- [15] He X, Zou Q, Luo LS, Dembo M. Analytic solutions of simple flows and analysis of nonslip boundary conditions for the lattice Boltzmann BGK model. *J Stat Phys* 1997;87:115–36.
- [16] Guo Z, Zheng C, Shi B. Discrete lattice effects on the forcing term in the lattice Boltzmann method. *Phys Rev E* 2002;65:046308.

- [17] Qian YH, D'Humières D, Lallemand P. Lattice BGK models for Navier–Stokes equation. *Europhys Lett* 1992;17:479–84.
- [18] Gong S, Cheng P, Quan X. Lattice Boltzmann simulation of droplet formation in microchannels under an electric field. *Int J Heat Mass Transfer* 2010;53:5863–70.
- [19] Kang Q, Zhang D, Chen S. Displacement of a two-dimensional immiscible droplet in a channel. *Phys Fluids* 2002;14:3203–14.
- [20] Kang Q, Zhang D, Chen S. Displacement of a three-dimensional immiscible droplet in a duct. *J Fluid Mech* 2005;545:41–66.
- [21] Sukop MC, Or D. Lattice Boltzmann method for modeling liquid–vapor interface configurations in porous media. *Water Resour Res* 2004;40:W01509.
- [22] Shan X, Doolen G. Multi-component lattice-Boltzmann model with interparticle interaction. *J Stat Phys* 1995;81:379–93.
- [23] Frisch U, d'Humières D, Hasslacher B, Lallemand P, Pomeau Y, Rivet JP. Lattice gas hydrodynamics in two and three dimensions. *Complex Syst* 1987;1:649–707.
- [24] Martys NS, Chen H. Simulation of multicomponent fluids in complex three-dimensional geometries by the lattice Boltzmann method. *Phys Rev E* 1996;53:743–50.
- [25] Hao L, Cheng P. Lattice Boltzmann simulations of liquid droplet dynamic behavior on a hydrophobic surface of a gas flow channel. *J Power Sources* 2009;190(2):435–46.
- [26] Zielke PCh, Szymczyk JA. Experimental investigation of the motion and deformation of droplets on surfaces with a linear wettability gradient. *Eur. Phys. J. Special Topics* 2009;166:155–8.
- [27] Manservigi S, Scardovelli R. A variational approach to the contact angle dynamics of spreading droplets. *Comput Fluids* 2009;38(2):406–24.
- [28] Gupta A, Kumar R. Droplet impingement and breakup on a dry surface. *Comput Fluids* 2010;39(9):1696–703.
- [29] Gupta A, Kumar R. Two-dimensional lattice Boltzmann model for droplet impingement and breakup in low density ratio liquids. *Comm. Comp. Phys.* 2011;10:767–84.
- [30] Gu X, Gupta A, Kumar R. Lattice Boltzmann simulation of surface impingement at high-density ratio. *J Thermophys Heat Transfer* 2009;23(4):773–85.
- [31] Yang Z L, Dinh TN, Nourgaliev RR, Sehgal BR. Numerical investigation of bubble growth and detachment by the lattice-Boltzmann method. *Int J Heat Mass Transfer* 2001;44(1):195–206.
- [32] Sukop MC, Thorne DT. *Lattice Boltzmann modeling: an introduction for geoscientists and engineers*. Berlin: Springer; 2006.
- [33] Aminfar H, Mohammadpourfard M. Lattice Boltzmann simulation of droplet base electrowetting. *Int J Comput Fluid Dyn* 2010;24(5):143–56.